Available online at www.sciencedirect.com
ScienceDirect
Ceramics International 35 (2009) 2587–2599
CERAMICS INTERNATIONAL
www.elsevier.com/locate/ceramint

Spark plasma sintering of self-propagating high-temperature synthesized $TiC_{0.7}/TiB_2$ powders and detailed characterization of dense product

Clara Musa [a,b], Antonio Mario Locci [a,b,*], Roberta Licheri [a,b], Roberto Orrù [a,b], Giacomo Cao [a,b,**], Dario Vallauri [c], Fabio Alessandro Deorsola [c], Elena Tresso [d], Jens Suffner [e,f], Horst Hahn [e,f], Piotr Klimczyk [g], Lucyna Jaworska [g]

[a] *Dipartimento di Ingegneria Chimica e Materiali, Unità di Ricerca del Consorzio Interuniversitario Nazionale per la Scienza e Tecnologia dei Materiali (INSTM), Università degli Studi di Cagliari, Piazza d'Armi, 09123 Cagliari, Italy*
[b] *Unità di Ricerca del Consorzio Nazionale delle Ricerche (CNR) – Dipartimento Energia e Trasporti, Università degli Studi di Cagliari, Piazza d'Armi, 09123 Cagliari, Italy*
[c] *Politecnico di Torino – Dipartimento Scienza dei Materiali, Corso Duca degli Abruzzi 24, 10129 Torino, Italy*
[d] *Politecnico di Torino – Dipartimento di Fisica, Corso Duca degli Abruzzi 24, 10129 Torino, Italy*
[e] *Joint Research Laboratory Nanomaterials, Technische Universität Darmstadt and Forschungszentrum Karlsruhe, Petersenstr. 23, 64287 Darmstadt, Germany*
[f] *Institute for Nanotechnology, Forschungszentrum Karlsruhe GmbH, Postfach 3640, 76021 Karlsruhe, Germany*
[g] *Institute of Advanced Manufacturing Technology, 3 a Wroclawska St., 30-011 Krakow, Poland*

Received 13 January 2009; received in revised form 23 January 2009; accepted 14 February 2009
Available online 11 March 2009

Abstract

In this work, the fabrication of bulk $TiC_{0.7}/TiB_2$ nanostructured composites through metastable transformation processing is investigated by taking advantages of two non-conventional powder metallurgy methods. First, the highly metastable $TiC_{0.7}/TiB_2$ agglomerated powders are synthesized by the so-called self-propagating high-temperature synthesis (SHS), followed by rapid quenching. Then, the spark plasma sintering (SPS) method is adopted to consolidate the SHSed powders.

A bulk ceramic composite with nanocrystalline microstructure characterized by a high-relative density is then obtained. Dwell temperature of 1400 °C, heating time of 3 min, and total processing time equal to 5 min, while applying a mechanical pressure of 20 MPa, are found to be the optimal SPS experimental conditions in order to obtain near-fully densified samples.

The obtained $TiC_{0.7}/TiB_2$ samples exhibit hardness HV5 as high as 24 GPa, modulus of elasticity of about 400 GPa, fracture toughness of about 5.6 MPa $m^{1/2}$, and a compressive strength of about 2.9 GPa. A very low-wear rate ($W_v = 3.8 \times 10^{-6}$ $mm^3/(N\,m)$) and a good thermal shock resistance ($\Delta T_c = 250$ °C) are also displayed. In addition, a high-abrasive wear factor (AWF) equal to 1.84 is evaluated on the basis of the achieved mechanical properties. These results make the obtained $TiC_{0.7}/TiB_2$ composite suitable for wear resistant parts as well as cutting tool materials.

Keywords: A. Powders: solid state reaction; A. Sintering; B. Nanocomposites; C. Mechanical properties

1. Introduction

The demand for materials exhibiting exceptional hardness and stability at very high temperature has led the interest in refractory materials such as the ceramic composite TiC/TiB_2 [1]. In fact, ceramic matrix composites (CMCs) offer considerable advantages over monolithic ceramics due to their enhanced fracture toughness and non-catastrophic failure behavior [2]. In addition, it is reported that the mechanical properties of the TiC/TiB_2 composite are superior than the weighted average of the properties of the monolithic TiC and TiB_2 [3].

* Corresponding author at: Dipartimento di Ingegneria Chimica e Materiali, Piazza d'Armi, 09123 Cagliari, Italy. Tel.: +39 070 6755072; fax: +39 070 6755057.
** Corresponding author at: Dipartimento di Ingegneria Chimica e Materiali, Piazza d'Armi, 09123 Cagliari, Italy. Tel.: +39 070 6755058; fax: +39 070 6755057.
E-mail addresses: antonio@visnu.dicm.unica.it (A.M. Locci), cao@visnu.dicm.unica.it (G. Cao).

0272-8842/$36.00
doi:10.1016/j.ceramint.2009.02.018

Besides to be suitable as high-temperature structural ceramics [1], such as components in heat exchangers and engines [4], other potential applications for TiC/TiB_2 composites include armor plates, wear-resistant elements in cutting tools, machine tool inserts, forming dies [1,4], water jet nozzles [5], first-wall tiles in nuclear fusion reactors, and vaporizing elements in vacuum metal deposition installations [4]. Beyond these properties, the ability to fabricate fully dense ultra-refractory TiC/TiB_2 ceramic/ceramic composites could result in a new class of materials that exhibit unique and attractive combinations of mechanical, electrical and magnetic properties [1]. For instance, due to its good electrical conductivity, TiC/TiB_2 has been proposed as cathode materials in Hall-Heroult cell for the electrolytic production of aluminum [1]. Another important consequence of the high-electrical conductivity is the possibility of the electro-discharge machining (EDM) of these otherwise difficult to form materials [2].

Development of nanostructured materials is a currently pursued strategy to improve the properties of ceramic composites. Specifically, nanostructured ceramic composites represent an attractive family of materials due to their outstanding properties such as superplasticity and enhanced mechanical behavior in terms of fracture toughness and wear resistance [6]. A successful processing route to obtain bulk nanostructured materials is based on the concept of metastability [7]. The idea is to synthesize ceramic composite powders that are inherently metastable and nanostructured, and that can be converted into a stable, fine-grained microstructure upon the re-crystallization occurring during the consolidation stage [8]. The condition for this approach applied to multiphase systems is that the components are either immiscible or nearly immiscible as solids, while maintaining varying degrees of extended solubility in their liquid state [9]. In fact, while the liquid constituents' miscibility gives the possibility to obtain a metastable structure through a rapid quench, the grain growth taking place during the sintering process may be limited by the near immiscibility of the constituent phases in the solid state [10]. In this framework, it appears that the ceramic composite TiC/TiB_2 may represent a promising candidate for the application of the strategy described above.

However, the melting temperatures of the constituents phases of the TiC/TiB_2 composites are very high, thus powder consolidation into full density bulk parts requires long exposures at extremely high-sintering temperatures and poses a real challenge [1,5], particularly if nanostructures must be preserved. Indeed, the high-processing temperatures adversely affect both microstructure and cost-effectiveness of these materials, and therefore more practical routes for fabricating dense TiC/TiB_2 parts are needed [2].

In this work, the fabrication of bulk $TiC_{0.7}$/TiB_2 nanostructured composite through metastable transformation processing is investigated by taking advantages of two non-conventional powder metallurgy methods. First, the highly metastable $TiC_{0.7}$/TiB_2 agglomerates powders are synthesized by the so-called self-propagating high-temperature synthesis (SHS) [11], followed by a rapid quench. Then, the spark plasma sintering (SPS) method is adopted to consolidate the SHSed powders. It should be noted that the SPS technique is reported to be able to shorten the sintering processing time [12,13] and hence, the limitation of the exposure to high temperatures, may help in avoiding grain growth during the consolidation step. In this way, the proposed processing route may represent a promising and versatile method to obtain nanostructured $TiC_{0.7}$/TiB_2 materials for a wide range of applications.

Specifically, after the description and discussion of the experimental conditions which lead to the fabrication of near-fully dense products, this paper is focused on the microstructural and mechanical characterization of the resulting samples. The obtained results are then compared to those reported in the literature for similar systems.

2. Experimental materials and methods

Flowchart of the overall process for the preparation of $TiC_{0.7}$/TiB_2 composites by metastable transformations is reported in Fig. 1. The first step consists in the achievement of nanocomposite $TiC_{0.7}$/TiB_2 powders by taking advantage of the concept of metastable transformations. The rapid cooling by quench of the SHS products allows one to obtain nanostructured powder agglomerates characterized by a high degree of metastability. The metastable powders are subsequently densified by SPS leading to bulk nanomaterials.

2.1. Powder preparation

The eutectic composition $TiC_{0.7}$/TiB_2 powders were prepared starting from Ti, B_4C and graphite by means of the SHS

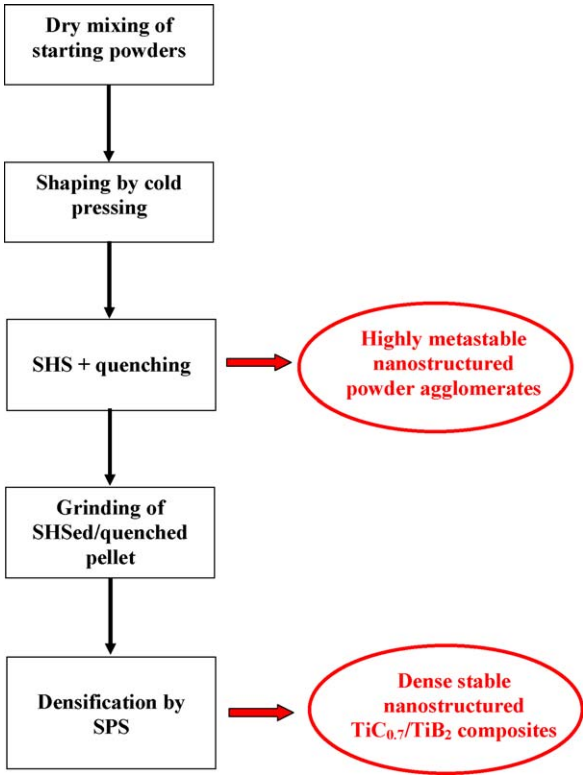

Fig. 1. Flowchart of the overall process for the preparation of $TiC_{0.7}$/TiB_2 composites by metastable transformations.

technique according to the following reaction [14]:

$$3Ti + 0.5B_4C + 0.9C \rightarrow 2TiC_{0.7} + TiB_2 \quad (1)$$

A specific process involving the synthesis of the $TiC_{0.7}/TiB_2$ composite through SHS followed by quench into a liquid bath has been designed [14]. The reacting pellet having 16 mm diameter and 5 mm height was supported by an aluminum foil (0.3 mm thickness) placed over a stainless steel cylinder (80 mm diameter) containing 50 cm^3 of water. The high temperature reached during the SHS process was sufficient to melt the foil when the combustion front reached the base of the pellet in contact with the foil. In this way, the reacted pellet was dropped into the quench bath that acts as quenching medium. In order to enhance the quenching efficiency, the reacting mixture was added with 1 wt.% of sodium borate ($Na_2B_4O_7{\cdot}10H_2O$) as gasifying agent. Additional details of the experimental materials, setup, and procedure as well as detailed results can be found elsewhere [14].

The experimental setup described above allowed for the production of highly metastable powder agglomerates of the nanostructured (nano–nano composite) $TiC_{0.7}/TiB_2$ material. Indeed, it should be also mentioned that the reaction stoichiometry (1) was chosen since a necessary condition to operate the described approach is that the maximum temperature reached during the SHS process is sufficiently high to generate the melting of the reaction products in order to induce metastability during quenching [14].

The SHS reacted pellets were milled for 3 h in a Fritsch Pulverisette 5 mill using a hardened steel 80 cm^3 vial with hardened steel balls (5 mm diameter) and setting up the charge ratio (ball to powder weight ratio) to 4. The powders were then ultrasonically dispersed and sieved below about 40 μm. A Malvern 2600/3600 (Malvern Instruments Ltd.) laser granulometry was used for the granulometric distribution measurement, while a Micromeritics ASAP 2010 equipment was used to determine the BET surface area of the powder by nitrogen adsorption–desorption at 77 K. Microstructural observations of the SHSed powders were carried out by field emission scanning electron microscope (FESEM) (Leo Supra 35) equipped with back-scattered electron (BSE) imaging and EDS/EDAX microprobe.

2.2. Powder consolidation

A SPS system (model 515S, Sumitomo Coal Mining Co. Ltd.) was used to produce dense samples starting from the $TiC_{0.7}/TiB_2$ powders synthesized by SHS and subsequently quenched. This apparatus combines a 50 kN uniaxial press with a DC pulsed current generator (10 V, 1500 A, 300 Hz) to simultaneously provide a pulsed electric current through the sample and the die containing it, together with a mechanical load through the die plungers. The adopted pulse cycle consisted of 12 pulses on and 2 pulses off, for a total pulse cycle duration equal to about 46.2 ms, with the characteristic time of a single pulse equal to about 3.3 ms.

Two types of SPS samples have been consolidated. For the preparation of samples hereafter labeled ''A'' about 3 g of powder were filled inside a graphite die (outside diameter, 30 mm; inside diameter, 15 mm; height, 30 mm). Samples hereafter labeled as ''B'' have been prepared by filling about 23.5 g into a graphite die having outside diameter of 35 mm, internal diameter of 16 mm, and height of 87 mm, respectively. In order to protect the dies and facilitate the sample release after synthesis, a 99.8% pure graphite foil (0.13 mm thick, Alfa Aesar) was inserted between the internal surface of the die and the sample and between the top and the bottom surface of the sample and the graphite plungers (14.7 mm diameter, 20 mm height, and 15.7 mm diameter, 36 mm height, when consolidating samples A and B, respectively). In addition, with the aim to minimize heat losses by thermal radiation, the dies were covered with a 2 mm thick layer of graphite felt (Atal s.r.l.). The dies were then placed inside the reaction chamber of the SPS apparatus and two cylindrical graphite spacers (80 mm diameter and 30 mm and both 40 mm high in the case of sample A) or one graphite disc (diameter 100 mm and 20 mm height in the case of sample B) were placed between the upper plunger and the upper electrode, as well as between the lower plunger and the lower electrode. Spacers, discs, dies and plungers were all made of AT101 graphite (Atal s.r.l.). Then, the system was evacuated down to about 20 Pa. This step was followed by the application of the mechanical pressure through the lower stainless steel electrode. The system was firstly heated from room temperature up to the dwell temperature T_D in a specified length of time (t_H) and then maintained at this temperature until a given total processing time t_T. At the end of the SPS process the application of the current was manually interrupted and the sample was first allowed to naturally cool and then removed from the die.

Temperature, root mean squared (RMS) applied current and voltage, mechanical load, and the vertical displacement of the lower electrode were measured in real time and recorded. In particular, temperatures were measured during the process by a C-type thermocouple (Omega Engineering Inc.), which was inserted inside a small hole on the lateral surface of the graphite die, while a specific data acquisition system was adopted to independently measure RMS current and voltage values [15].

2.3. Bulk samples characterization

The relative density of the product was determined by helium pycnometry (Pycnomatic, Porotec GmbH) averaging 20 density values and Archimedes method using distilled water as wetting liquid. Phase identification in SPS samples was performed with Cu Kα radiation (λ = 1.540598 Å) by using a D8 X-ray diffractometer (Bruker-AXS) equipped with an energy-dispersive Sol-X detector. The phase contents and crystallite sizes have been determined by Rietveld refinement by means of the TOPAS software (Bruker-AXS). The microstructure of the densified products was examined by high-resolution scanning electron microscopy (HR-SEM) using a XL30 FEG (Philips) equipped with an EDX detector (EDAX).

Mechanical properties such as hardness, Young's modulus, fracture toughness, bending and compressive strength, friction coefficient and wear rate were also evaluated. Specifically, Vickers microhardness (HV0.3) has been determined using an indentation load of 2.94 N/mm^2 (300 mg) and a holding time of 15 s. The average microhardness was evaluated from at least 15 indents for each sample. Knoop's hardness measurements were also performed and a load of 9.81 N was applied. Five hardness measurements were carried out for each sample.

Bending bars with dimensions of about 3 mm × 4 mm × 25 mm have been obtained by cutting SPS sample B using a diamond wheel saw followed by grinding and polishing with diamond spray down to 1 μm grain size to obtain coplanar surfaces. These bars were then used to determine the Young's modulus by the impulse excitation technique according to the ASTM C 1259-94. The samples were placed on rubber foam and excited with a small flexible hammer. The excited ultrasonic spectrum is recorded with a microphone and the first harmonic frequency f_g is automatically calculated. Based on the knowledge of the materials' density and geometry, the Young's modulus E can be calculated for bar shaped samples through standard equations.

The elasticity constant E of material was determined also by the ultrasonic method, according to the following formula:

$$E = \rho C_T^2 \frac{3C_L^2 - 4C_T^2}{C_L^2 - C_T^2} \tag{2}$$

where C_L is the velocity of the longitudinal wave, C_T is the velocity of the transversal wave, and ρ is the material density. The velocities of transversal and longitudinal waves were determined as the ratio of the sample thickness and the relevant transition time. Considering that the error in the thickness measurements and in the time-of-flight measurements were ±0.01 mm and ±1 ns, respectively, the resulting error in the ultrasonic velocity was about 1%. Uncertainty of ρ measurements is 0.02 g/cm^3. Consequently, the accuracy of Young's modulus calculated from Eq. (2) could be estimated to be 2%.

The same bars adopted for the determination of E were also used to perform bending tests that were carried out in a setup having an outer roll distance of 20 mm and an inner roll distance of 10 mm. The force was transferred over the upper rolls to the bending bar, inducing a constant bending moment in between the inner rolls. The load was applied within a second until fracture occurs and the maximum force was recorded. The bending strength was calculated using a standard equation. The edges of the bar have been chamfered to remove any defects that have been introduced during sample preparation like cutting and grinding.

Compression tests at room temperature have been performed on specimens with the dimensions of 3 mm × 3 mm × 4.5 mm obtained by cutting the SPS sample B. The compression testing machine continuously loads the sample with a constant strain rate while strain and force are recorded until rupture of the material occurs. Samples have been ground on all sides to prepare parallel surfaces. The load at rupture divided by the starting cross-sectional area A_0 is defined as the compression strength σ_c.

The fracture toughness was calculated from the length of cracks that develop during a Vickers indentation test through the Niihara's equation:

$$\left(\frac{K_{IC}\varphi}{Ha^{1/2}}\right)\left(\frac{H}{E\varphi}\right)^{2/5} = 0.129\left(\frac{c}{a}\right)^{-3/2} \tag{3}$$

where K_{IC} is the critical stress intensity factor, φ is the constrain factor, H is the Vickers hardness, E is the Young's modulus, and a the half of indent diagonal. For this determination a load of 49 N was adopted. Five hardness measurements were carried out for each sample.

Wear tests for the evaluation of the coefficients of friction μ for the contact with Si_3N_4 ball were performed while temperature in the materials ball–disc contact zone and specific wear rate according to wear volume were determined. The ball-on-disc tests were carried out without lubricant according to ISO 20808:2004(E). The friction force was measured continuously during the test using the force sensor FT-5102 (Spais). Temperature in the ball and disc contact zone was measured using a Thermo-Hunter PT-3S infrared thermometer (Optex Ltd.). For each test a new ball was used. Specimens were washed in high-purity acetone and dried. After ball and sample were mounted, materials were washed in ethyl alcohol and then dried. The disc shaped SPS samples A was used for these friction tests after lapping and polishing by means of diamond wheels. For all samples roughness was measured through the Hommel Tester-T1000E contact instrument. Specifically, the following parameters were determined: the arithmetic average of the absolute values of the roughness profile, R_a, and the arithmetic mean value of the single roughness depth of consecutive sampling lengths, R_z.

The ball specimen is a sphere of 1 mm diameter with a roughness not exceeding 0.1 μm. Due to the SPS samples size limitation the following parameters were established: applied load, 1 N; sliding speed, 0.1 m/s; diameter of the sliding circle, 5 mm; sliding distance, 100 m; number of cycles, 3200. The values of friction coefficient was calculated from the following equation:

$$\mu = \frac{F_f}{F_n} \tag{4}$$

where F_f is the measured friction force, and F_n is the applied normal force. For the wear track on the disc specimen, the cross-sectional profile of the wear track at four places at intervals of 90° using a contact stylus MCT System profilometer (CSEM Inc.) was evaluated with accuracy of measurement of 0.01 μm and of 0.1 μm in the vertical and horizontal axis, respectively. The cross-sectional area of the wear track was calculated using an custom-developed software. Specific wear rate according to wear volume was calculated by means of equation:

$$W = \frac{V_{sample}}{F_n L} \tag{5}$$

where V_{sample} is the wear volume of the disc specimen (mm^3), F_n is the applied load (N), and L is the sliding distance (m). The former parameter was evaluated as follows:

$$V_{sample} = \pi R \frac{(S_1 + S_2 + S_3 + S_4)}{2} \quad (6)$$

where R is the radius of wear track (mm), and S_1–S_4 represent cross-sectional areas at four places on the wear track circle (m^2). The specific wear rate of the ball specimen according to wear volume was evaluated by means of equation:

$$W_b = \frac{V_{ball}}{F_n L} \quad (7)$$

being the volume of the ball given by

$$V_{ball} = \pi \frac{A^3 B}{32D} \quad (8)$$

where D is the diameter of ball specimen (mm), and A and B (both in mm) are the minimum diameter and the diameter in a direction perpendicular to it, respectively, which were measured using a micrometer microscope (Neophot).

The thermal shock behavior of the $TiC_{0.7}/TiB_2$ SPS samples A was evaluated by quenching them into water, according to the EN 820-3:2004 specifics. The inspection after quenching was connected with mechanical tests in order to evaluate the loss of strength with increasing initial temperature or using the determination of the presence of defects by dye penetration test (EN 623-1). A set of test pieces was heated to a given temperature, and then quickly and smoothly transferred to a water bath. The test pieces were inspected for cracks or other damage by using a penetrating dye to detect the presence of cracks. The apparatus consisted of: (a) temperature-controlled oven (JMM K25B) capable of maintaining a set of test pieces at a given temperature ±5 °C; (b) suitable test piece holder capable of being transferred rapidly from oven to the quenching medium within 0.5 s; (c) water bath controlled at 20 ± 2 °C and of sufficient volume so that the net temperature rise after quenching the test pieces is less than 5 °C. The temperature of the pieces in the oven is record by PtRh30–PtRh6 thermocouple (Alfasensor).

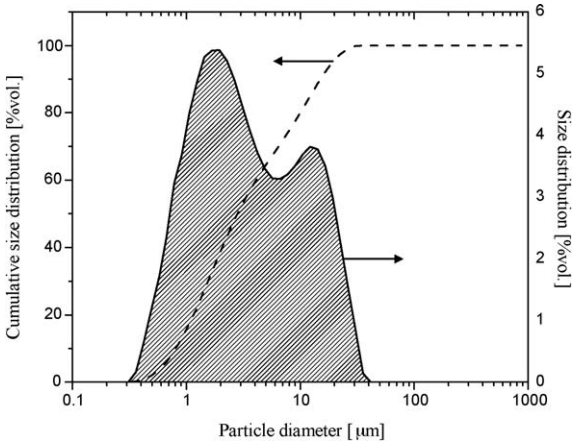

Fig. 2. Cumulative and granulometric size distribution of $TiC_{0.7}/TiB_2$ powders synthesized by SHS + quenching.

The samples for the thermal shock tests were polished using diamond wheels and slurry. Then they were placed in the oven and heated slowly to a temperature near to that which is expected to induce failure after quenching. After a period of at least 10 min during which the temperature of the test samples becomes stable, it was recorded. The test pieces were transferred to the water bath. Samples were removed and dried after a minimum period of 2 min. The development of surface cracks were investigated by means of scanning electron microscope JEOL JSM-6460LV. The temperature range for thermal shock tests was 250–800 °C, which is covered with 25 °C increments.

3. Results and discussion

3.1. Powders characterization

The XRD pattern of the powder synthesized by SHS + quenching revealed that the product is mainly constituted by the desired TiC_x and TiB_2 phases with small amount of unreacted titanium. The lattice parameter calculated from indexing patterns of cubic TiC_x crystal is $a = 4.3247$ Å, which corresponds to a value of x equal to 0.7, as expected from the adopted SHS reaction stoichiometry. The results of the particle size distribution analysis of the SHSed/quenched powders are shown in Fig. 2. The reported cumulative and differential granulometric size distribution curves indicate that the obtained powder is characterized by particles smaller than 40 μm, and in particular, the 90 vol.% is finer than 20 μm. The specific surface area resulted to be about 4.9 m^2/g. Microstructural observations by SEM of the powders formed during the SHS + quench process showed the formation of powder agglomerates characterized by fine structures, as reported elsewhere [14,16,17].

Fig. 3 shows the analysis carried out by EDS mapping of the elements where an intimate level of mixing of the two constituent phases $TiC_{0.7}$ and TiB_2 can be noticed. The results of the confocal laser scanning microscopy (CLSM) analysis on the powders are reported in Figs. 4 and 5. The CLSM technique allows a 3D representation of the powder agglomerates, which shows the formation of nanostructured grains occurred during the SHS + quench process. In addition, a certain degree of metastability of the SHSed/quenched product was observed as verified by subsequent thermal treatments [14]. In particular, the metastability was confirmed by the morphological transformation of the nanostructures induced by heating.

3.2. Powders densification

The optimization of the experimental conditions for densification of the $TiC_{0.7}/TiB_2$ powders by SPS has been performed by using sample A. The experimental parameters along with the obtained results in terms of density are summarized in Table 1. It can be seen that in order to obtain a sample characterized by near-full density the dwell temperature had to be increased up to 1400 °C. It should be noted that at the lowest temperature investigated, an increase of the applied

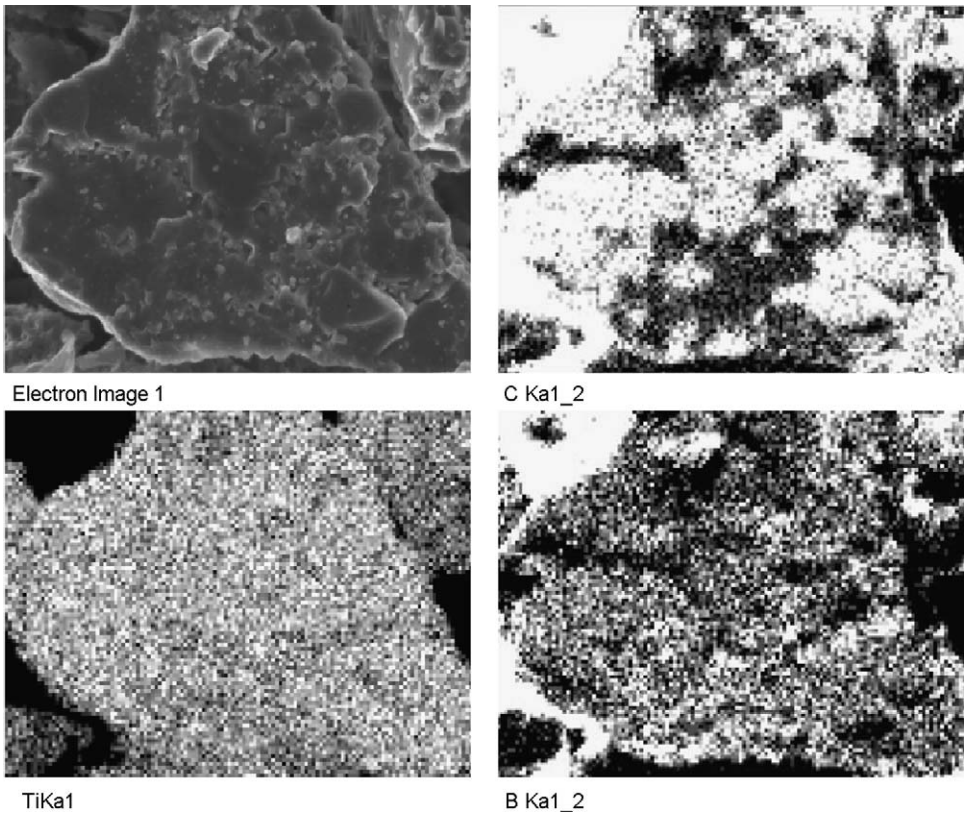

Fig. 3. Microstructure and EDS mapping of the powder agglomerates of $TiC_{0.7}/TiB_2$ composites powder obtained by SHS + quenching.

mechanical pressure from 20 to 50 MPa did not result in significant changes of the sample density. Therefore, a heating time of 3 min, a total time of 5 min, and a dwell temperature of 1400 °C while applying a mechanical pressure of 20 MPa represent the optimal experimental SPS conditions in order to obtain fully densified samples. The same conditions were then applied to prepare B samples.

The displacement profile recorded during the SPS densification of $TiC_{0.7}/TiB_2$ powders when adopting the optimized experimental conditions is shown in Fig. 6. It can be seen that during the first 60 s ($T < 400$ °C), the displacement does not show any significant variation. As a consequence of the temperature increase, the displacement increases to about 0.5 mm in the next 30 s, indicating a first compaction of the powders due the particle re-arrangement facilitated by the temperature increase. This first stage of densification is completed very quickly, and the displacement remains constant until the temperature reaches about 750–800 °C ($t = 120$ s). Then, the sintering stage begins and the displacement increases thus reaching its maximum after 240 s of electric current application. It can be seen from Fig. 6 that the consolidation due to the sintering phenomena occurs in the temperature range 800–1200 °C with its maximum rate at about $T = 1100$ °C. The observed increase of the displacement when the application of the electric current is interrupted is a manifestation of the shrinkage of the sample ensemble (electrodes/blocks/spacers/die/plungers/sample) due to thermal shrinkage accompanying the cooling of the system.

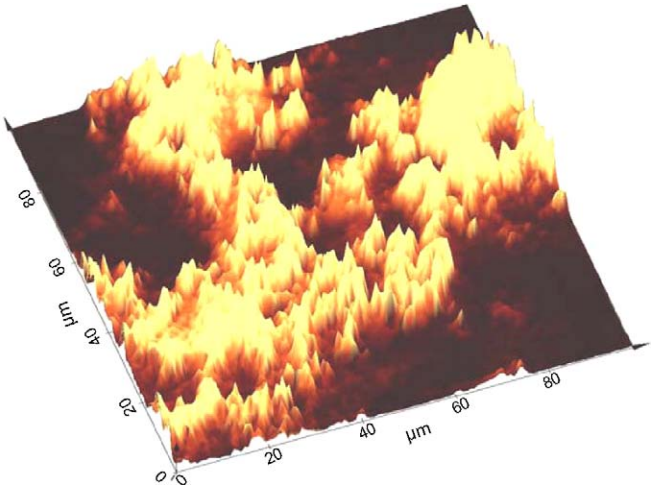

Fig. 4. Confocal laser scanning microscopy image of the powder agglomerates of $TiC_{0.7}/TiB_2$ composites obtained by SHS + quench.

For sake of comparison, in Table 2 the experimental conditions adopted for the consolidation of TiC_x/TiB_2 composite by different powder metallurgy methods, along with the corresponding starting powders, are shown. It should be noted that the optimal experimental conditions adopted in this work to achieve a fully dense composite are among the milder ones reported in the literature. Specifically, mechanical pressure as low as the one applied during the present investigation has been adopted only by Lis et al. [5]. However, it was necessary to increase the temperature up to 1800 °C to obtain fully dense samples. In addition to the temperature,

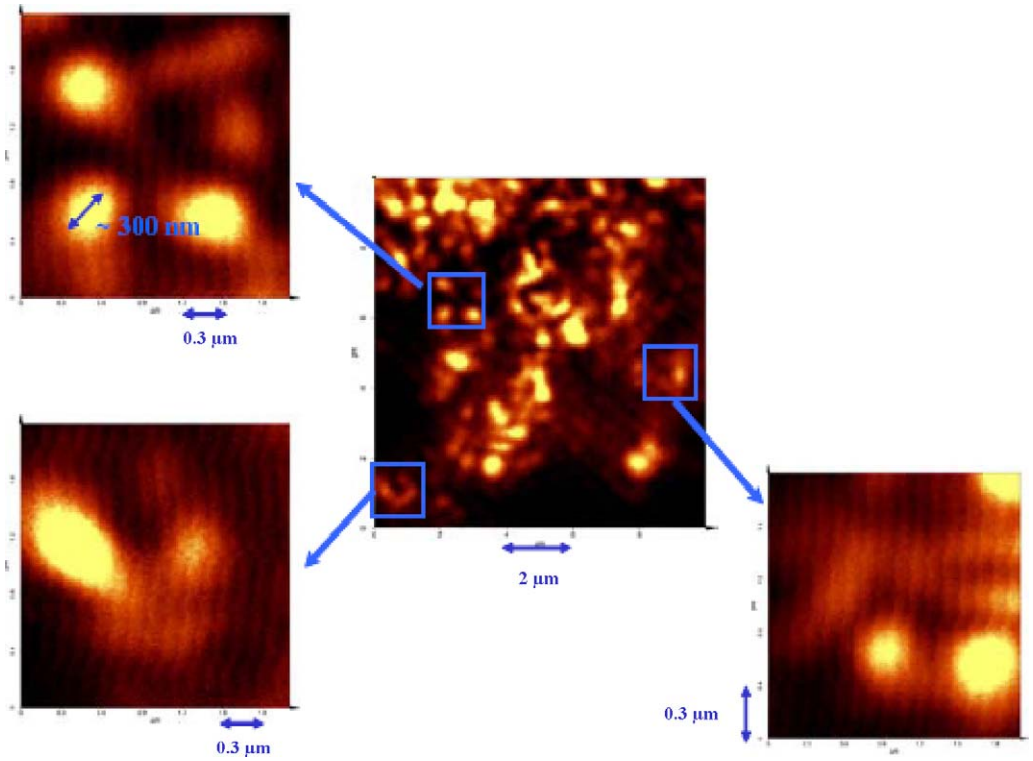

Fig. 5. Confocal laser scanning microscopy image of the powder agglomerates of $TiC_{0.7}/TiB_2$ composites obtained by SHS + quench.

which is significantly higher than that one optimized in the present work, also processing time is longer. Regarding the sintering temperature, only in the field activated pressure assisted synthesis (FAPAS) process [25], it was comparable with the one adopted in this work. However, a slightly higher applied mechanical pressure and longer processing time were needed with respect to the optimal experimental conditions defined in this work.

A further analysis of the data reported in Table 2 leads to the conclusion that, except for those processes characterized by few seconds of processing time, where the densification is carried out simultaneously with the combustion synthesis of the composite or the application of pressure of the order of GPa is involved, the optimal processing time resulting from this investigation is among the shorter ones. In particular, near- or full dense TiC–TiB_2 are obtained only by Gotman et al. [2] and Locci et al. [28,29] through simultaneous synthesis and sintering of reactant powders. However, in the former investigation the applied mechanical pressure has been increased up to 150 MPa, while in the latter one the temperature has been brought up to 1700–1800 °C.

Table 1
Experimental conditions adopted during the SPS processing of the SHSed/quenched $TiC_{0.7}/TiB_2$ powders, and corresponding density values.

T_D (°C)	P (MPa)	t_H (min)	t_T (min)	Density (g/cm^3)	Relative density (%)
1200	20	3	5	4.545	97.1
1200	50	3	5	4.508	96.3
1300	20	3	5	4.525	96.7
1400	20	3	5	4.807	>99.9

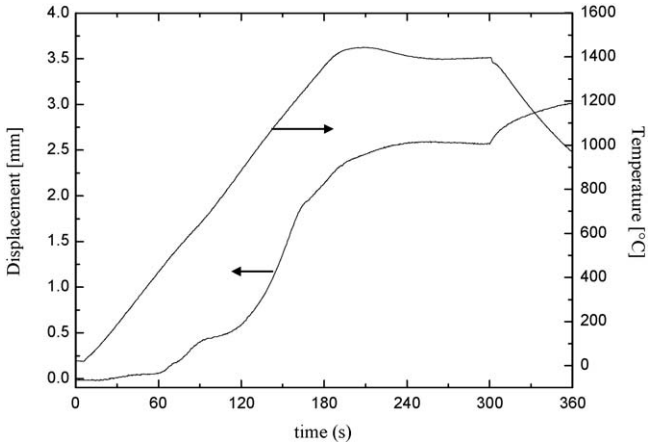

Fig. 6. Displacement and temperature time profiles recorded during the spark plasma sintering of the $TiC_{0.7}/TiB_2$ composite SHSed/quenched powders.

The results illustrated above can be taken as an indication of the higher sinterability of the powder produced by the SHS process investigated in this work and/or the sintering phenomena rates enhancement due to the electric current flowing during the SPS process. It should be mentioned that, while coherently limiting the comparison to the investigations where consolidation of already-synthesized TiC–TiB_2 powders was performed, the apparent higher sinterability shown by the powders produced in this work does not seem to be a consequence of particle size level. Indeed, powders sintered

Table 2
Summary of experimental conditions and corresponding relative density values available in the literature of bulk TiC_x/TiB_2 composite obtained by means of different processes.

Composite	Starting powders	Consolidation method	Applied pressure (MPa)	Sintering temperature (°C)	Processing time (s)	Relative density (%)	Reference
$TiC + 2TiB_2$	Commercial Ti and B_4C	Hot pressing	41	1600	38,400	92	[1]
$TiC + 2TiB_2$	Commercial TiC and TiB_2	Hot pressing	20	1800	3600	100	[5]
$TiC + 2TiB_2$	Combustion synthesized TiC and TiB_2	Hot pressing	20	1800	1800	100	[5]
$TiC + 2TiB_2$	Combustion synthesized TiC and TiB_2	Pressureless sintering	–	2050	3600	100	[5]
$4TiC + TiB_2$	Commercial Ti, B, and C	SHS under pressure	150–200	–	25	94.5	[18]
$3TiC + 2TiB_2$	Commercial Ti, B, and C	SHS under pressure	150–200	–	25	92.5	[18]
$2TiC + 3TiB_2$	Commercial Ti, B, and C	SHS under pressure	150–200	–	25	93.5	[18]
$TiC + 2TiB_2$	Commercial Ti and B_4C	TE under pressure	150	1000	60	100	[2]
$TiC + 2TiB_2$	Commercial Ti and B_4C	Hot pressing	150	1100	14,400	95	[2]
$9TiC + TiB_2$	Commercial Ti, $B_{13}C_2$, and C	SHS/shock consolidation	–	–	20–90	91.5	[19]
$4TiC + TiB_2$	Commercial Ti, $B_{13}C_2$, and C	SHS/shock consolidation	–	–	20–90	91.5	[19]
$4.998TiC + TiB_2$	Commercial Ti, C, and TiB_2	Hot pressing	60–70	1600	38,400	>99	[20]
$2.976TiC_{0.5} + TiB_2$	Commercial Ti, C, and TiB_2	Hot pressing	60–70	1600	38,400	>99	[20]
$TiC_{0.5} + 1.176TiB_2$	Commercial Ti, C, and TiB_2	Hot pressing	60–70	1600	38,400	>99	[20]
$2.957TiC_{0.56} + TiB_2$	Commercial Ti, C, and TiB_2	Hot pressing	60–70	1600	38,400	>99	[20]
$5.062TiC_{0.57} + TiB_2$	Commercial Ti, C, and TiB_2	Hot pressing	60–70	1600	38,400	>99	[20]
$TiC + 2TiB_2$	Commercial Ti, B_4C, and C	SHS/shock consolidation	–	–	<20	>98	[21]
$2TiC + TiB_2$	Commercial Ti, B_4C, and C	SHS/shock consolidation	–	–	<20	85.5	[21]
$TiC + 5.667TiB_2$	Commercial TiC and TiB_2	Hot isostatic pressure	3000	2250–2500	300	98.2–99.3	[3]
$TiC + 5.667TiB_2$	Commercial Ti, B, and C	Hot isostatic pressure	3000	2250	5–300	98.5–99.1	[3]
$TiC + 5.667TiB_2$	Commercial Ti, B, and C	Hot isostatic pressure	3000	2500	300	99	[3]
$3TiC + 2TiB_2$	Combustion synthesized TiC and TiB_2	Hot pressing	30	1800	3600	99.7	[22]
$TiC + TiB_2$	Combustion synthesized TiC and TiB_2	Hot pressing	30	1800	3600	99.8	[22]
$2TiC + 3TiB_2$	Combustion synthesized TiC and TiB_2	Hot pressing	30	1800	3600	99.6	[22]
$TiC + 2TiB_2$	Commercial Ti, B_4C	Hot pressing	30	1800	3600	97	[23]
$TiC_{0.5} + 2TiB_2$	Commercial Ti, B_4C	Hot pressing	30	1700–1800	3600	94–100	[23]
$TiC + 2TiB_2$	Commercial Ti, B_4C, and C	SHS under pressure	160	–	<20	96.1	[24]
$TiC + TiB_2$	Commercial Ti, B_4C, and C	SHS under pressure	160	–	<20	91.2	[24]
$2TiC + TiB_2$	Commercial Ti, B_4C, and C	SHS under pressure	160	–	<20	93.1	[24]
$TiC + TiB_2$	Ball milled Ti, B, and C	FAPAS	30	1400	600	98.6	[25]
$TiC_{0.5} + TiB_2$	Commercial Ti and B_4C	Hot pressing	35	1800	3600	>98	[26]
$TiC + TiB_2$	Commercial Ti, B_4C, and C	SPS	20	1800	240	100	[28]
$TiC + TiB_2$	Ball milled Ti, B_4C, and C	SPS	20	1700	240	98	[29]
$2TiC_{0.7} + TiB_2$	Combustion synthesized $TiC_{0.7}$ and TiB_2	SPS	20	1400	300	100	This work

during other investigations [3,5] had particle size in the range 1.5–2.5 and 8.3–9.5 μm, respectively. On the other hand, the sintered powders particle size was not reported by Lee et al. [25]. However, it is worth mentioning that the latter ones were mechanically treated by ball milling up to 10 h, which makes reasonably to presume a fine particle size. Therefore, it is possible to recognize that powders consolidated in this work are the coarser ones (cf. Fig. 2) with respect to the comparable literature.

3.3. Microstructural characterization of bulk samples

The ceramic composite $TiC_{0.7}/TiB_2$ was successfully densified by spark plasma sintering also when the samples B was subjected to the same optimal conditions adopted for the case of sample A. Material density has been determined in this case to be 4.747 ± 0.003 g/cm^3 that corresponds to a relative density of 98.75%. Phase composition of sample B has been investigated by X-ray diffraction as shown in Fig. 7, where the XRD pattern of the starting SHSed powders is also shown for sake of comparison. The sample contains 62.9 wt.% of $TiC_{0.7}$ phase and 36.2 wt.% of TiB_2, as estimated by Rietveld analysis. A small amount (0.9 wt.%) of metallic α-Ti has been also identified in the sample. Grain size of both constituent phases as well as lattice parameter a of the cubic TiC_x cell, has been determined by means of the Rietveld refinement of the XRD pattern. The crystallite size of the $TiC_{0.7}$ and TiB_2 are 32 and 70 nm, respectively. Furthermore, the lattice parameter was evaluated equal to 4.3035 Å, which is smaller than the one given in the reference ICSD #151365 ($a = 4.3150$ Å), thus confirming that the TiC phase is non-stoichiometric.

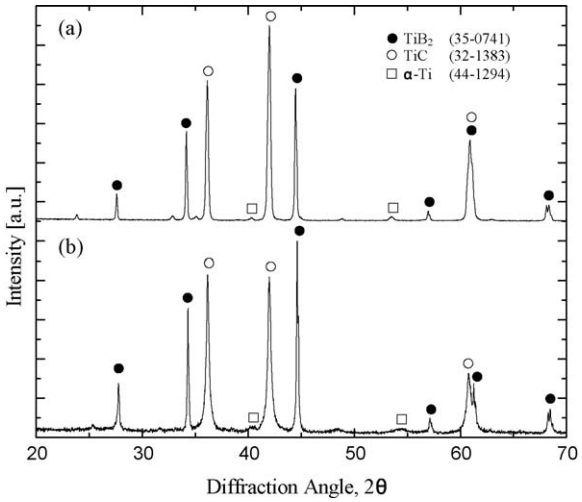

Fig. 7. XRD patterns of (a) $TiC_{0.7}/TiB_2$ samples densified by SPS and (b) starting $TiC_{0.7}/TiB_2$ SHSed/quenched powders, respectively.

The microstructure at different magnification of the polished cross-sections of SPS sample B as found by SEM is displayed in Fig. 8(a)–(c). In the latter one, it can be seen that the grain size of both phases appearing in the microstructure is about 1 μm. By comparing this evidence with the results obtained by the Rietveld analysis of the XRD pattern, it can be stated that the micrograins appearing in Fig. 8(c) are constituted by nanocrystallites. On the basis of EDX spectroscopy analysis the darker grains are identified as TiB_2 while the light gray ones correspond to the $TiC_{0.7}$ phase. Fig. 9 shows the fractured surfaces of the SPS sample after 4-point bending, where it can be observed that fracture occurs and propagates at grain boundary. However, also intragranular fracture was occasionally observed, preferably through the larger, TiB_2 grains.

3.4. Mechanical characterization of bulk samples

Vickers hardness (HV0.3) of sample B has been determined to be 24.13 ± 2.49 GPa. A summary of the mechanical properties of the TiC_x/TiB_2 composites taken from the literature is reported in Table 3. It can be see that the hardness of the $TiC_{0.7}/TiB_2$ composite obtained in this work is comparable to, and in some cases results higher than the ones reported in the literature.

The fracture toughness values of TiC_x/TiB_2 composite reported in the literature are also summarized in Table 3. The fracture toughness of both SPS samples A and B has been evaluated equal to 5.6 MPa $m^{1/2}$. It can be therefore stated that the K_{IC} obtained in this work is comparable with the ones reported in Table 3, except for some significantly [23,29] or exceptionally [23,26] higher values.

The Young's modulus is about 373 and 401 GPa for samples A and B respectively, which are comparable with the values of 460 and 350 GPa obtained by Broadkin et al. [20] for the composite $TiC_{0.5}/1.176TiB_2$ and $5.062TiC_{0.57}/TiB_2$, respectively. It should be pointed out that the latter ones are the only E values reported in the literature for the TiC_x/TiB_2 system. The bending strength of the $TiC_{0.7}/TiB_2$ composite obtained in this work is 93 ± 46 MPa. This value is lower than those reported in

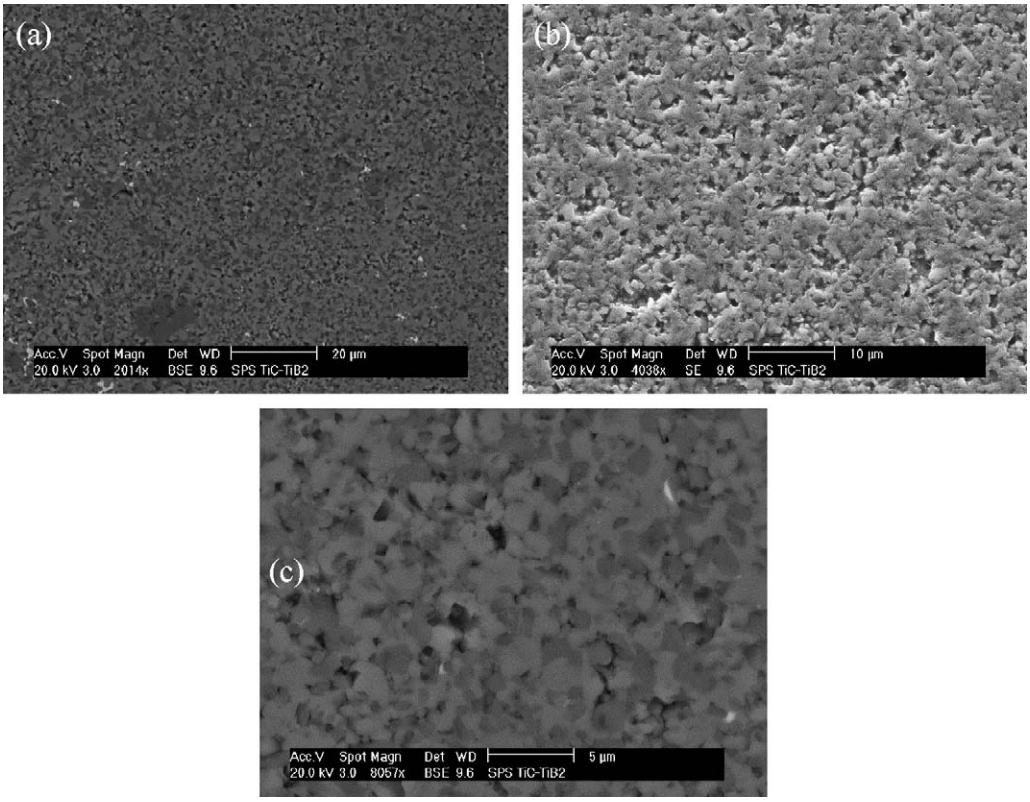

Fig. 8. (a–c) Back-scattered electron (BSE) micrographs at different magnifications of $TiC_{0.7}/TiB_2$ samples densified by SPS.

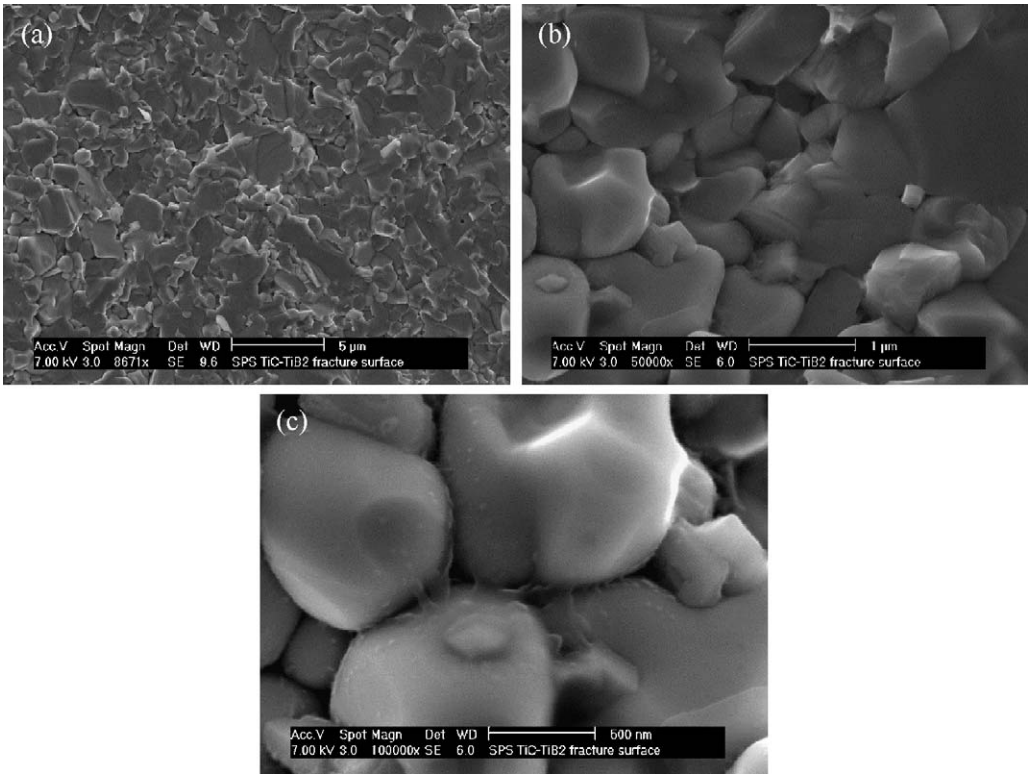

Fig. 9. (a–c) SEM micrographs at different magnification of the fracture surface of $TiC_{0.7}/TiB_2$ samples densified by SPS.

the literature, which typically fall in the range from 100 to 700 MPa (cf. Table 3). This discrepancy can be due to several reasons. In particular, samples B are characterized by a relatively high length/diameter ratio, so that some inhomogeneities inside the specimen might arise during sintering. This aspect, along with the very high-heating rate adopted in order to keep the nanosized structure during the SPS process, might lead to the measured low-bending strength, being the latter ones very sensitive to flaws in the materials like large pores or grains.

Regarding the compression test performed, Fig. 10 displays an example of the corresponding curve, where it can be seen that after equilibration of the contact points, the sample deforms almost elastically until fracture occurs. An average value for the strength under compressive loading of 2937 ± 317 MPa has been obtained. Compressive strength values were reported in the literature only by Zhang et al. [24], which obtained 2.6, 2.1, and 2.4 GPa for $TiC/2TiB_2$, TiC/TiB_2, and $2TiC/TiB_2$ composites, respectively. It can be clearly stated that these values of σ_c are slightly smaller with respect to the one obtained in this work.

Friction and wear test were carried out on SPS samples A and the results of friction coefficient and temperature measurements for the sample and the Si_3N_4 balls methods are presented in Fig. 11. During the first stage, the friction coefficient increases slowly from the initial value of 0.1 up to about 0.13 when the number of the cycles reaches 500. In the next stage (from 500 to 1500 cycles), a rapid increasing of the friction coefficient up to 0.7 takes place. Next, the latter one remains approximately constant so that its value does not change significantly up 3200 cycles. In the same figure, temperature measurements shows only small linear increasing of the temperature (from 20 to 35 °C) in the Si_3N_4 ball and the composite disc contact zone.

A summary of the related results is reported in Table 4, while the morphology of the wear tracks on samples after sliding is shown in Fig. 12. On the basis of the features of wear in the ball contacts areas appearing in this figure, the material obtained in this work should be classified as abrasive. The results of the wear tests highlighted that the $TiC_{0.7}/TiB_2$ SPS composite obtained was characterized by a very low-wear rate ($W_v = 3.8 \times 10^{-6}$ mm^3/(N m)).

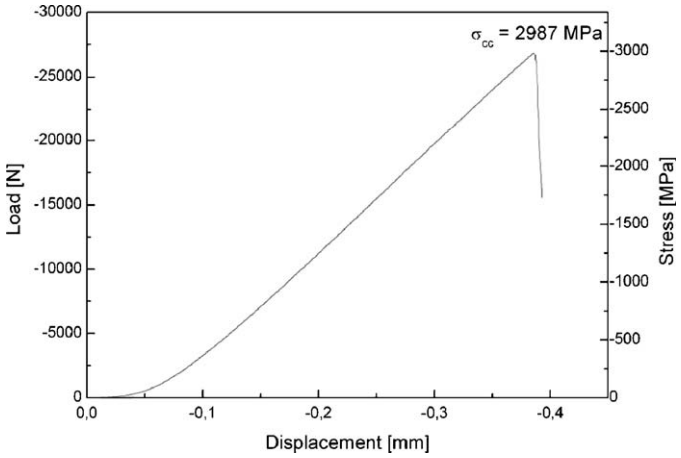

Fig. 10. Load vs. displacement curve obtained from compression test of the $TiC_{0.7}/TiB_2$ samples densified by SPS.

Table 3
Summary of mechanical properties of bulk TiC_x/TiB_2 composites reported in the literature.

Composite	Hardness	K_{IC}	σ_f	Notes	Reference
$TiC + 2TiB_2$	18–24	4–5	100	HV0.3	[1]
$TiC + 2TiB_2$	29.5	–	–	HV1	[5]
$4TiC + TiB_2$	93.5	–	700	HRC	[18]
$3TiC + 2TiB_2$	93	–	650	HRC	[18]
$2TiC + 3TiB_2$	93.5	–	560	HRC	[18]
$TiC + 2TiB_2$	20.6–25.4	5.9–6.6	190–210	HV0.5	[2]
	15.1–16.2			HV20	
$9TiC + TiB_2$	16	–	–	HV0.5	[19]
$4TiC + TiB_2$	13	–	–	HV0.5	[19]
$4.998TiC + TiB_2$	–	–	526	–	[20]
$2.976TiC_{0.5} + TiB_2$	23	–	498	HV10	[20]
$TiC_{0.5} + 1.176TiB_2$	16	–	430	HV10	[20]
$2.957TiC_{0.56} + TiB_2$	16	–	500	HV10	[20]
$5.062TiC_{0.57} + TiB_2$	–	–	525	–	[20]
$TiC + 2TiB_2$	3200	–	–	HK0.1	[21]
	1600			HK5	
	1600			HK10	
$TiC + 5.667TiB_2$	22.6–23.9	3.5–4.6	–	HV0.2	[3]
$3TiC + 2TiB_2$	93.2	4.81	456	HRA	[22]
$TiC + TiB_2$	92.9	5.53	383	HRA	[22]
$2TiC + 3TiB_2$	93	5.48	378	HRA	[22]
$TiC + 2TiB_2$	–	8.44	453.9	–	[23]
$TiC_{0.5} + 2TiB_2$	–	8.58–12.2	504.6–680.4	–	[23]
$TiC + 2TiB_2$	93.25	5.64	440	HRA	[24]
$TiC + TiB_2$	85.9	5	–	HRA	[24]
$2TiC + TiB_2$	92	3.75	410	HRA	[24]
$TiC + TiB_2$	20.6	–	–	HV0.4	[25]
$TiC_{0.5} + TiB_2$	25	12.5	680.4	HV10	[26]
$4TiC + TiB_2$	27.4	3	–	HV0.1	[27]
	27.1			HV0.2	
	26.3			HV0.5	
	24.2			HV1	
$2.571TiC + TiB_2$	25.6	4	–	HV0.1	[27]
	25.3			HV0.2	
	24.2			HV0.5	
	22.2			HV1	
$2TiC + 3TiB_2$	25	4	–	HV0.1	[27]
	24.5			HV0.2	
	23			HV0.5	
	19.9			HV1	
$TiC + TiB_2$	2500		–	HK0.1	[28]
$TiC + TiB_2$	18.5–19.5	6.94–7.73	–	HV20	[29]
$2TiC_{0.7} + TiB_2$	24.13	5.6	93	HV0.3	This work

The microstructure of SPS sample A after thermal shock at the critical quenching temperature difference (ΔT_c) of 250 °C is shown in Fig. 13. While ΔT_c values for TiC_x/TiB_2 composites have not been reported in the literature, the $\Delta T_c = 250$ °C measured in this work for the $TiC_{0.7}/TiB_2$ composite resulted slightly higher than the 150–200 °C reported by Wayne and Buljan [30] for the competing Al_2O_3–TiC material.

As mentioned above, one of the potential applications of the TiC_x/TiB_2 composites is cutting tool inserts. A criterion for comparing the wear resistances of different ceramics has been proposed by taking advantage of the abrasive wear factor (AWF) [31], which can be computed from the knowledge of fracture toughness (K_{IC}), Young's modulus (E), and hardness (H) values as follows:

$$AWF = \frac{K_{IC}^{0.5} H^{1.43}}{E^{0.8}} \quad (9)$$

The higher the AWF, the higher is the expected resistance of ceramics to abrasive wear. The AWF of the $TiC_{0.7}/TiB_2$ composites obtained in this work is 1.84. Unfortunately, a direct comparison of this parameter with other TiC/TiB_2 composites cannot be made because the complete set of mechanical properties necessary to evaluate the AWF is not available for each material. However, the value obtained in this work favorably compares for instance to the similar $TiC–TiB_2–Ti_3B_4$ composites obtained by Broadkin et al. [20] which display an

Table 4
Summary of friction and wear tests results.

Property	Value	Units
R_a	0.05	μm
R_z	0.48	μm
μ	0.72	–
Width of wear track	153.6	μm
Depth of wear track	0.13	μm
Cross-sectional area of wear track	12.2	μm^2
W_v	3.8×10^{-6}	$mm^3/(N\ m)$
A	235	μm
B	242	μm
W_b	3.08×10^{-6}	$mm^3/(N\ m)$

AWF = 1.26, and to commercial Al_2O_3–TiC, SiAlON, and WC/TiC/Co cutting tool materials which show wear factors of 1.22, 1.21, and 0.95, respectively [20,32].

Further investigations are needed to clarify whether the very high AWF is due to high density, small crystallite size, or material composition, or the combination of such properties which characterized the composite obtained in this work.

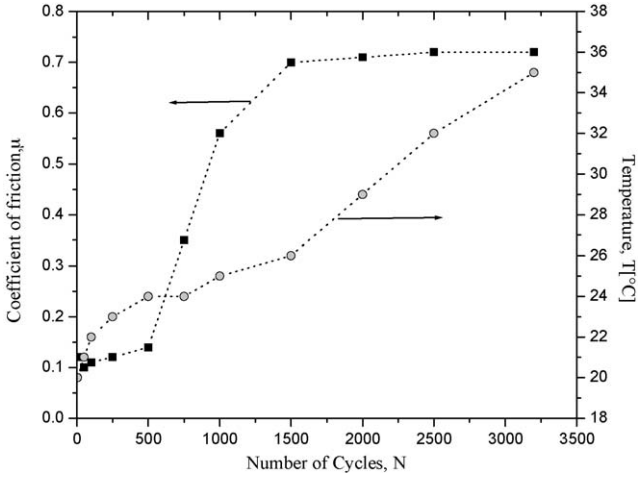

Fig. 11. Coefficient of friction and temperature of Si_3N_4 ball and specimen contact zone for SPS sample A.

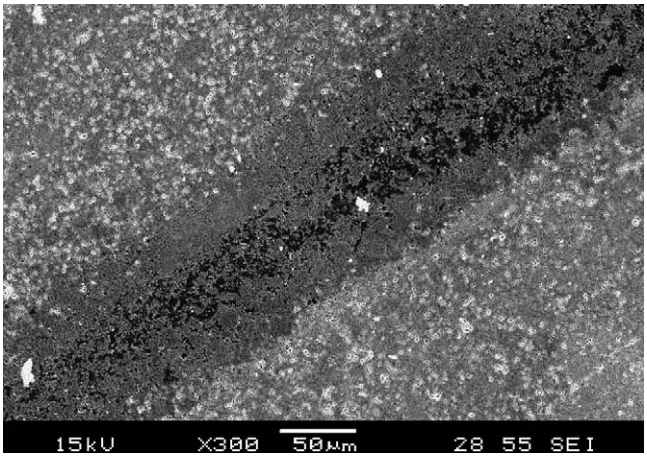

Fig. 12. Scanning electron micrograph of the worn contact area after wearing tests for SPS sample A and Si_3N_4 ball material.

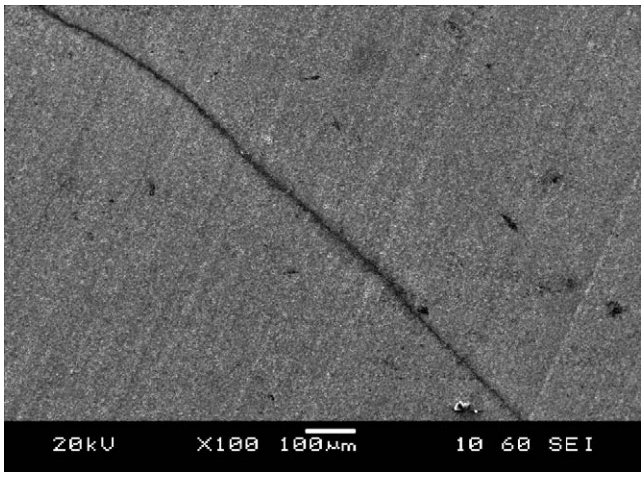

Fig. 13. Scanning electron micrograph of SPS sample A after thermal shock at temperature $\Delta T_c = 250\ ^\circ C$.

4. Concluding remarks

The results of the microstructural and mechanical characterization of the $TiC_{0.7}/TiB_2$ samples densified by SPS starting from metastable powders produced by SHS are presented in this work. It has been shown that the obtained material is characterized by a high-relative density along with a nanocrystalline microstructure.

Dwell temperature of 1400 °C, heating time of 3 min, and total processing time equal to 5 min, while applying a mechanical pressure of 20 MPa, were found to be the optimal SPS experimental conditions in order to obtain near-fully densified samples. By comparing the experimental conditions reported in the literature for the consolidation of TiC_x/TiB_2 composite by different powder metallurgy methods, it can be seen that the ones optimized in this work are among the most convenient. This result can be taken as an indication of the high sinterability that characterizes the powder produced by SHS and/or the sintering rate enhancement due to the electric current flowing through the sample during SPS processes.

$TiC_{0.7}/TiB_2$ samples having hardness as high as 24 GPa, modulus of elasticity of about 400 GPa, fracture toughness of about 5.6 MPa $m^{1/2}$, and a compressive strength of about 2.9 GPa have been obtained. A very low-wear rate ($W_v = 3.8 \times 10^{-6}\ mm^3/(N\ m)$) and a good thermal shock resistance ($\Delta T_c = 250\ ^\circ C$) were also determined. In addition, a high AWF equal to 1.84 can be evaluated on the basis of the achieved mechanical properties. The good combination of the latter ones makes the $TiC_{0.7}/TiB_2$ composite obtained by the processing route investigated in this work suitable for wear resistant parts and application as cutting tool material as demonstrated by the favorable comparison with competing state-of-the-art materials.

Acknowledgement

The financial support of NAMAMET project (NMP3-CT-2004-001470), EU is gratefully acknowledged.

References

[1] M.W. Barsoum, B. Houng, Transient plastic phase processing of titanium boron carbon composites, Journal of the American Ceramic Society 76 (6) (1993) 1445–1451.
[2] I. Gotman, N.A. Travitzky, E.Y. Gutmanas, Dense in situ TiB_2/TiN and TiB_2/TiC ceramic matrix composites—reactive synthesis and properties, Materials Science & Engineering A 244 (1) (1998) 127–137.
[3] S.K. Bhaumik, C. Divakar, A.K. Singh, G.S. Upadhyaya, Synthesis and sintering of TiB_2 and TiB_2–TiC composite under high pressure, Materials Science & Engineering A 279 (1–2) (2000) 275–281.
[4] D. Brodkin, S.R. Kalidindi, M.W. Barsoum, A. Zavaliangos, Microstructural evolution during transient plastic phase processing of titanium carbide–titanium boride composites, Journal of the American Ceramic Society 79 (7) (1996) 1945–1952.
[5] J. Lis, S. Majorowski, V. Hlavacek, J.A. Puszynski, Combustion synthesis and densification of TiB_2–TiC composite powders, International Journal of Self-Propagating High-Temperature Synthesis 4 (3) (1995) 275–285.
[6] G.M. Chow, N.I. Noskova, Nanostructured Materials, Kluwer Academic, Amsterdam, 1998, pp. 47–70.
[7] B.H. Kear, Z. Kalman, R.K. Sadangi, G. Skandan, J. Colaizzi, W.E. Mayo, Plasma-sprayed nanostructured Al_2O_3/TiO_2 powders and coatings, Journal of Thermal Spray Technology 9 (4) (2000) 483–487.
[8] J.M. Wu, Z.Z. Li, Nanostructured composite obtained by mechanically driven reduction reaction of CuO and Al powder mixture, Journal of Alloys and Compounds 299 (2000) 9–16.
[9] B.H. Kear, J. Colaizzi, W.E. Mayo, S.C. Liao, On the processing of nanocrystalline and nanocomposite ceramics, Scripta Materialia 44 (8–9) (2001) 2065–2068.
[10] S.C. Liao, J. Colaizzi, Y. Chen, B.H. Kear, W.E. Mayo, Refinement of nanoscale grain structure in bulk titania via a transformation-assisted consolidation (TAC) method, Journal of the American Ceramic Society 83 (9) (2000) 2163–2169.
[11] A. Varma, A.S. Rogachev, A.S. Mukasyan, S. Hwang, Combustion synthesis of advanced materials: principles and applications, Advances in Chemical Engineering 24 (1998) 79–225.
[12] T. Nishimura, M. Mitomo, H. Hirotsuru, M. Kawahara, Fabrication of silicon nitride nano-ceramics by spark plasma sintering, Journal of Materials Science Letters 14 (1995) 1046–1047.
[13] N. Tamari, T. Tanaka, K. Tanaka, I. Kondoh, M. Kawahara, M. Tokita, Effect of spark plasma sintering on densification and mechanical properties of silicon carbide, Journal of the Ceramic Society of Japan 103 (1995) 740–742.
[14] D. Vallauri, I.C. Atías-Adrián, F.A. Deorsola, I. Amato, B. DeBenedetti, Metastability route to obtain nanocomposites by SHS, International Journal of Self-Propagating High-Temperature Synthesis 15 (2) (2006) 169–179.
[15] A. Cincotti, A.M. Locci, R. Orrù, G. Cao, Modeling of spark plasma sintering/synthesis apparatus: temperature, current and strain distribution with no current, AIChE Journal 53 (3) (2007) 703–719.
[16] D. Vallauri, Y. López, B. DeBenedetti, I. Amato, Nanocomposite TiC–TiB_2 powders by SHS through metastability approach, Advances in Science and Technology 45 (2006) 1005–1010.
[17] I.C. Atías-Adrián, D. Vallauri, Z. Zhang, A. Chrysanthou, B. DeBenedetti, I. Amato, Nanostructured TiC_{1-x}–TiB_2 composites obtained by metastability processing, Advanced Materials Research 15–17 (2006) 225–230.
[18] E.A. Levashov, V.I. Kosayanin, L.M. Krukova, J.J. Moore, D.L. Olsen, Structure and properties of Ti–C–B composite thin films produced by sputtering of composite TiC–TiB_2 targets, Surface and Coatings Technology 92 (1997) 34–41.
[19] R. Tomoshige, Y. Kakoki, K. Imamura, A. Chiba, Effect on addition of titanium diboride to titanium carbide produced by the SHS shock consolidation method, Journal of Materials Processing & Technology 85 (1–3) (1999) 105–108.
[20] D. Brodkin, A. Zavaliangos, S.R. Kalindindi, M.W. Barsoum, Ambient- and high-temperature properties of titanium carbide–titanium boride composites fabricated by transient plastic phase processing, Journal of the American Ceramic Society 82 (3) (1999) 665–672.
[21] I. Song, L. Wang, M. Wixom, L.T. Thompson, Self-propagating high temperature synthesis and dynamic compaction of titanium diboride/titanium carbide composites, Journal of Materials Science 35 (10) (2000) 2611–2617.
[22] R. Yuan, Z. Fu, W. Wang, H. Wang, SHS TiB_2-based multiphase ceramics and composites, International Journal of Self-Propagating High-Temperature Synthesis 10 (4) (2001) 435–450.
[23] G. Wen, S.B. Li, B.S. Zhang, Z.X. Guo, Reaction synthesis of TiB_2–TiC composites with enhanced toughness, Acta Materialia 49 (8) (2001) 1463–1470.
[24] X.H. Zhang, C.C. Zhu, W. Qu, X.D. He, V.L. Kvanin, Self-propagating high temperature combustion synthesis of TiC/TiB_2 ceramic–matrix composites, Composites Science & Technology 62 (15) (2002) 2037–2041.
[25] J.W. Lee, Z.A. Munir, M. Ohyanagi, Dense nanocrystalline TiB_2–TiC composites formed by field activation from high-energy ball milled reactants, Materials Science & Engineering A 325 (1–2) (2002) 221–227.
[26] S.B. Li, B.S. Zhang, G. Wen, J.X. Xie, Microstructure and mechanical properties of platelet-reinforced Ti–B–C ceramics prepared by reaction hot pressing of B_4C and Ti powders, Materials Letters 57 (8) (2003) 1445–1452.
[27] W.J. Li, R. Tu, T. Goto, Preparation of directionally solidified TiB_2–TiC eutectic composites by a floating zone method, Materials Letters 60 (2006) 839–843.
[28] A.M. Locci, R. Orrù, G. Cao, Z.A. Munir, Simultaneous spark plasma synthesis and densification of TiC–TiB_2 composites, Journal of the American Ceramic Society 89 (3) (2006) 848–855.
[29] A.M. Locci, R. Orrù, G. Cao, Z.A. Munir, Effect of ball milling on simultaneous spark plasma synthesis and densification of TiC–TiB_2 composites, Materials Science & Engineering A 434 (1–2) (2006) 23–29.
[30] S.F. Wayne, S.T. Buljan, The role of thermal shock on tool life of selected ceramic cutting tool materials, Journal of the American Ceramic Society 72 (5) (1989) 754–760.
[31] A.G. Evans, D.B. Marshall, Wear mechanism in ceramics, in: ASM Fundamental of Friction and Wear Materials, ASM International, Metals Park, USA, 1980, pp. 439–452.
[32] G.S. Upadhayaya, Materials science of cemented carbides—an overview, Materials Design 22 (2001) 483–489.